ACS APPLIED MATERIALS & INTERFACES

www.acsami.org Research Article

Modality-Tunable Exfoliated N-Doped Graphene as Effective Electrolyte Additive for High-Performance Lithium−Sulfur Batteries

Vaidik R. Shah, Ritwick Sinha, Walter J. Cesarski, Xiaosi Gao, Simuck F. Yuk, and Yong Lak Joo*

Cite This: *ACS Appl. Mater. Interfaces* 2024, 16, 53950−53962 **Read Online**

ACCESS | Metrics & More | Article Recommendations | Supporting Information

Downloaded via CORNELL UNIV on October 21, 2024 at 18:17:27 (UTC).
See https://pubs.acs.org/sharingguidelines for options on how to legitimately share published articles.

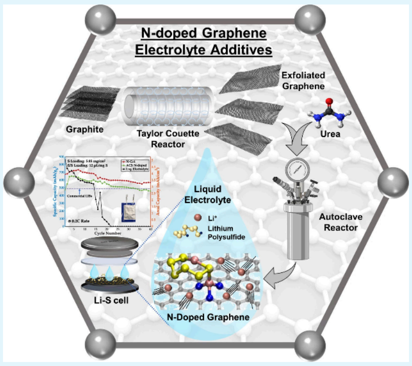

ABSTRACT: While chemically doped graphene has shown great promise, the lack of cost-effective manufacturing has hindered its use. This study utilizes a facile fabrication approach for modality-tunable N-doped graphene via thermal annealing of aqueous-phase-exfoliated few-layered graphene from a Taylor−Couette reactor. This method demonstrates a high level of N-doping (27 atom % N) and offers modality tunability of the C−N bond without foregoing scalability and green chemistry principles. The resulting N-doped graphene, with varying N content and doping modality, is utilized in the lithium−sulfur battery electrolyte to address low ionic conductivity, lithium polysulfide (LiPS) shuttling, and Li anode instability. The study reveals that higher N content and pyridinic N modality graphene in the electrolyte positively influence battery performance. The results are 2-fold: higher overall N content improves capacity retention (73%) after 225 cycles at 0.2 C, and pyridinic-type nitrogen demonstrates the best performance at high C rates, exhibiting a 4-fold capacity increase relative to the reference cell at 2 C. Further, the computational study validates the adsorption affinity of LiPS to pyridinic nitrogen and improved Li^+ mobility on the graphene backbone observed experimentally. This first experimental study on the impact of N-dopant concentration and modality on electrochemical performance provokes insights into tailoring N functionalization to achieve superior electrochemical performance.

KEYWORDS: *Taylor−Couette exfoliated graphene, nitrogen-doped graphene, electrolyte additives, lithium−sulfur battery, DFT and ab initio MD simulations*

INTRODUCTION

While Li-ion batteries (LIB) maintain their dominance as the current commercial standard for energy storage, the burgeoning demand for larger capacities and superior energy densities has necessitated the need to look beyond traditional LIB technology. To that effect, lithium−sulfur (Li−S) batteries, with their ultrahigh theoretical energy density of about 2600 Wh kg^{-1} and abundant, environmentally benign sulfur (S) cathodes, are seen as promising replacements to achieve energy densities beyond 500 Wh kg^{-1}. Despite these advantages, the practical applications of Li−S technology are limited by severe capacity decay and low Coulombic efficiency, owed largely to the shuttle of dissolved polysulfides (Li_2S_n, $4 \leq n \leq 8$) and the insulating nature of sulfur (S) and Li_2S (final discharge product).[1,2]

To address these challenges, a multitude of approaches have been investigated. Widely adopted strategies include some form of cathodic S-encapsulation modifications, such as designing advanced conducting cathodic matrices to confine LiPS via physical encapsulation,[3,4] spraying conducting polymer/carbon-supported layers to retard LiPS diffusion,[5,6] incorporating redox mediators compounds to chemically confine LiPS and improve redox kinetics,[7,8] incorporating exotic organic and inorganic-based solid-state electrolytes,[9,10] and separator modifications in the form of composite layering of LiPS adsorbant polymers,[11,12] carbon-based species,[13,14] porous MOFs,[15,16] and complex ion-selective inorganic membranes[17] to trap dissolved PS and suppress shuttling. Though innovative and successful at the lab scale, these approaches fail to show promise at commercial scales largely due to the high economic stress of utilizing exotic materials and the additional complexity and costs associated with cell fabrication.[18,19] Innovation in low-cost materials and a scalable, facile cell fabrication protocol are necessary to truly realize the commercialization of Li−S technology.

In recent years, graphene, a two-dimensional carbon nanomaterial with fascinating properties, including high theoretical surface area (2630 m^{-2} g^{-1})[20] and rapid charge carrier mobility (200000 V^{-1} s^{-1}),[21] has received interest for potential use in various applications such as supercapacitors[22] and high-density energy storage.[20] However, due to an almost

Received: July 21, 2024
Revised: September 4, 2024
Accepted: September 19, 2024
Published: October 1, 2024

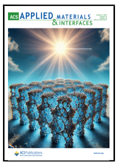

ACS Publications © 2024 American Chemical Society

https://doi.org/10.1021/acsami.4c12157

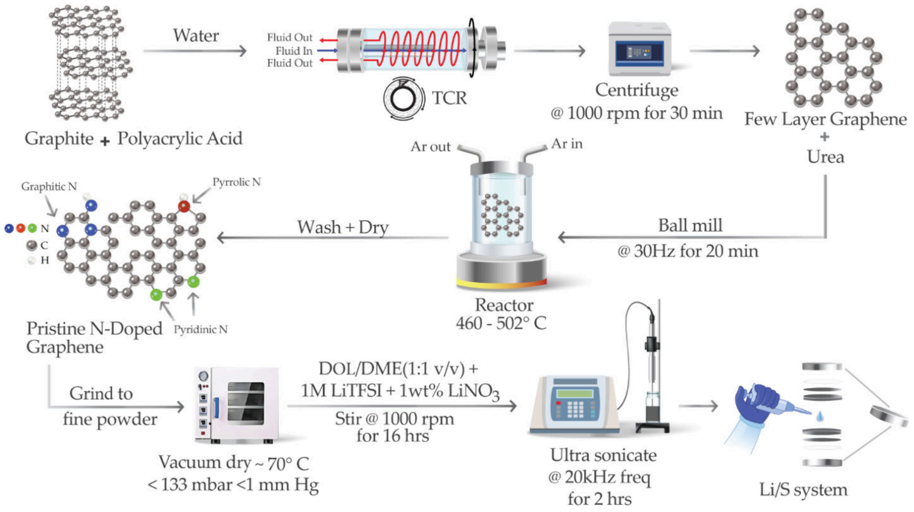

Figure 1. Overall process schematic illustrating graphene exfoliation, N-doping, and Li/S cell fabrication.

gapless band structure, the scope for direct application has been limited. Heteroatomic doping is an effective approach for tailoring graphene properties conducive to the battery and nanoelectronic devices. While boron, sulfur, and phosphorus doping are common, nitrogen-doped graphene (N-Gr), synthesized by directly substituting carbon atoms in the graphitic lattice, demonstrates interesting electronic conductivity[23] and chemical interaction properties.[24] For instance, the Fermi level of an N-doped graphene system is shifted above the Dirac point,[25] thus suppressing the density of states function near the Fermi level. This opens a gap between the valence and conductance bands, making it effective for electrochemical applications. Another potential advantage is that the charge distribution of carbon atoms is altered by nearby higher electronegative nitrogen atoms,[26] creating an activation region suitable for heterocatalytic reactions[27] or tethering polar nanoparticles like LiPS in Li−S systems.[28] Several studies have demonstrated N doping in carbonaceous materials as an efficient strategy to enhance the electrochemical performance of Li−S cells.[29,30] Zhang et al. fabricated a Li plating matrix and showed that N-containing functional groups, such as pyridinic and pyrrolic nitrogen in N-Gr, are lithophilic and guide metallic Li nucleation and suppress dendrite growth.[31] Wang et al. demonstrated that N-doped graphene frameworks showed great effectiveness in supercapacitor and electrocatalysis applications.[32] Fu et al. reported a methodology to construct an electrochemically recoverable protective layer of polysulfides using N-doped carbon dots; they posited that the N doping reacted with the LiPS to form a solid, recoverable polysulfide encapsulating layer, hence arresting LiPS shuttling.[33]

Due to the atomic size similarity of carbon and nitrogen, direct synthesis of N-Gr via chemical vapor deposition (CVD) is common[34] yet expensive, as it forgoes scalability. Other common methods include segregation growth,[35] arc discharge,[36] plasma treatment,[37] hydrazine treatment,[38] and thermal treatment of reduced graphene oxide (r-GO).[39] However, most, if not all, of these methods require harsh energy-draining conditions and flammable organic gases and/or toxic organic solvents, making them both environmentally and economically untenable. Herein, we introduce a facile N-doped graphene-based electrolyte additive solution toward the goal of achieving high-performance Li−S batteries. We have performed thermal annealing of low-defect TCR exfoliated graphene, with urea as the nitrogen source, to produce samples of N-Gr with highly tunable N at. % between 7−27% on the surface with facile modality control between different N-dopant configurations pyridinic, pyrrolic, and quaternary.[40] In addition to obtaining large amounts of functionalized graphene, this protocol allows for the streamlined synthesis of N-Gr by using a green approach. The pristine graphene itself is produced by continuous high shear-induced exfoliation of synthetic graphite in an aqueous medium,[41] which forgoes the organic solvents and enumerable stabilizers commonly used.[42] The setup is designed to be scaled as necessary for industrial applications. The structure and composition of prepared N-Gr were confirmed by Raman spectroscopy, X-ray photoelectron spectroscopy (XPS), elemental analysis (CHNX analysis), scanning electron microscopy (SEM), energy-dispersive X-ray spectroscopy (EDS), X-ray diffraction (XRD), thermogravimetric analysis (TGA), and Brunauer−Emmett−Teller (BET) surface area analysis.

In this work, we successfully report N-doped graphene as an effective electrolytic additive for Li−S batteries. In doing so, we have also evaluated the performance of our prepared N-Gr additives relative to reference Li−S electrolyte and commercial N-Gr as an additive. Further, this study, to the best of our knowledge, reports the first approach toward comparing the relevant electrochemical performance trends associated with changing N-dopant concentration and modality on the graphene framework. Our investigation suggests that the graphenic network in the electrolyte facilitates the Li^+ conductions and hence enhances ionic conductivity and improves cell redox kinetics, leading to improved cycling performance and stability, long cycle life, and better high-rate capability. Further, we show that the N dopants show affinity toward charged LiPS moieties, leading to a reduced polysulfide shuttle and, subsequently, a suppressed capacity fade and higher Coulombic efficiencies. Additionally, post-mortem analysis of the anodes shows a more homogeneous Li surface morphology and a significant absence of dendritic growth post long-term cycling, which may be ascribed to better regulation of Li nucleation on the anode due to Li−N interactions at the anode/electrolyte interface. Battery testing revealed that cells prepared by the mere addition of N-Gr electrolyte additives show a high reversible capacity of 897 mAh g_S^{-1} at 0.5 C, a low

https://doi.org/10.1021/acsami.4c12157
ACS Appl. Mater. Interfaces 2024, 16, 53950−53962

cycling capacity fade of 0.13% per cycle, and a remarkable improvement in the rate capability of the cells—a 3-fold and 4-fold higher capacity than reference at 1 C (628 mAh g_S^{-1}) and 2 C (369 mAh g_S^{-1}), respectively.

Computationally, researchers have used density functional theory (DFT) calculations to study the binding energies of LiPS species with different configurations of polysulfides. Though there is variability in the exact mechanism of binding proposed, most of the studies show a heightened LiPS interaction with N-doped species, leading to improved LiPS immobilization.[43−45] Despite the plethora of computational investigations, there is limited experimental exploration of the impact of the amount and modality of N-doping on the electrochemical performance of the Li−S system, especially via an electrolyte additive approach. To that end, we used DFT and *ab initio* molecular dynamics (AIMD) simulations to elucidate our experimental observations and theoretically explore the influence of different nitrogen sites on shuttling effects and have successfully demonstrated the adsorption affinity of pyridinic nitrogen groups on the graphene surface to lithium polysulfides, thus limiting LiPS shuttling and improving the overall electrochemical cell performance.

RESULTS AND DISCUSSION

Sample Preparation and Characterization. While thermal annealing with NH_3 is an established method for the doping of N onto the surface of graphene layers, it usually results in a low at. % of N, a consequence of very high annealing temperatures.[46] Coupled with the fact that the graphene used for doping is usually synthesized using a modified form of the Hummers method,[47] the process is unviable for industrial-scale synthesis. The proposed process in the present study, which involves the continuous shear-induced exfoliation of graphite in aqueous media, followed by doping using urea, is not only cost-effective but also green in that it foregoes the use of organic solvents. Figure 1 is an illustration of the overall process.

Four different doped graphene samples (N-Gr 1, N-Gr 2, N-Gr 3, and N-Gr 4) were prepared using different ratios (by weight) of exfoliated graphene and urea at different reaction times and annealing temperatures. Figure 2a−f shows SEM (scanning electron microscopy) images of the graphitic precursor, exfoliated graphene, and nitrogen-doped graphene. The exfoliation process results in the formation of large lateral dimension (>10 μm), flat thin sheets (E-Gr = 14.36 μm, N-Gr 1 = 13.56 μm, N-Gr 2 = 13.04 μm, N-Gr 3 = 12.17 μm, and N-Gr 4 = 8.95 μm; Figure S1, Supporting Information), and the doping process preserves this morphology.

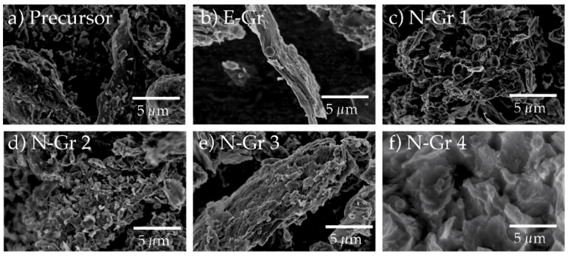

Figure 2. Surface morphology of graphene flakes. SEM images show the difference in morphology between (a) graphitic precursor and (b) exfoliated graphenic sheets. SEM also displays the consistent morphology of (c) N-Gr1, (d) N-Gr 2, (e) N-Gr-3, and (f) N-Gr 4.

The chemical composition and doping modalities were studied by using X-ray photoelectron and energy-dispersive X-ray spectroscopy (Figure 3a−d). EDS spectra show a uniform distribution of nitrogen on the surface of the graphene flakes. The high-resolution N 1s spectra of NGr 1−4 (Figure 3a−d) were deconvoluted into two primary peaks centered at 398 ± 0.5 and 400 ± 0.4 eV, which indicate pyridinic (N_{prn}) and pyrrolic (N_{pyr}) bonding modalities, respectively. This bonding modality could be altered by changing reaction parameters (nitrogen precursor mass, temperature, and annealing time), making the process highly tunable. It was experimentally observed that the low reaction temperature processes (<500 °C), with longer times taken to reach reaction temperature, resulted in lower nitrogen doping (by at. %) but higher levels of pyridinic-type nitrogen bonding. This is the case for N-Gr 1 and N-Gr 2, which were synthesized under such conditions. The spectrum of N-Gr 3 also revealed a higher binding energy peak at 401 eV, characteristic of graphitic bonding of nitrogen (N_{gr}). Higher reaction temperature processes, such as the one used to synthesize N-Gr 4, show higher levels of N doping (by at. %) but an almost equal ratio of pyrrolic to pyridinic-type nitrogen bonding. The chemical compositions as well as reaction parameters of N-Gr 1−4 are tabulated in Table 1. For N-Gr 1, however, the peaks corresponding to pyrrolic and graphitic modalities, after deconvolution, appeared to be within the margin of error of the instrument. It can be safely assumed that N-Gr1 (Figure 3a) comprises purely pyridinic graphene. Additional syntheses are listed in Table S8. The N-bonding modality was further studied using the C 1s high-resolution XPS spectra. Upon analysis of N-Gr 1, the primary peaks were ascertained to be the 284.1 and 284.8 eV peaks, corresponding to sp^2 C−C bonding in the graphene lattice. The other peaks correspond to sp^2 C═N (285.9 eV), sp^3 C−N, and sp^3 C−O (287.8 eV). Beyond 291 eV, the observed feature is a result of a $\pi-\pi$ shake-up process (Figure S2).

The chemical structure of the doped graphene was further studied by means of Raman spectroscopy. As shown in Figure 4a, Raman spectra (E_{Laser} = 532 nm) of graphite precursor (GP), exfoliated graphene (E-Gr), and the nitrogen-doped samples (N-Gr) have three distinct reflexes, corresponding to the D (1350 cm^{-1}) band, G (1570 cm^{-1}), and the 2D (2700 cm^{-1}) band, respectively.[41] A fourth reflex, the D′ (1620 cm^{-1}), can also be observed, albeit not distinct. It can be observed that while the exfoliation results in the blue-shift of both the G band (from 1567 to 1581 cm^{-1}) and the D band (1345−1360 cm^{-1}), N-doping results in the blue-shifting of only the D band, with higher levels of blue-shift for higher doping levels by at. % (Figure 4b). The D band corresponds to structural changes to the graphite lattice, and exfoliation results in higher intensity.[41] It is observed that the introduction of N atoms to the graphenic plane results in an increase in the intensity of the D band to levels comparable to those of the G band. This is indicative of higher structural defect as a result of heteroatom doping on both the plane and the edge, which can be confirmed by the increase in the defect levels, as characterized by an increase in I_D/I_G ratio with N doping (Figure S5). A blue-shift in the D reflex is also observed. The D reflex, indicative of a local defect, is another metric to identify doping. As different modalities of N bonding exist on the graphenic plane, it must be noted that their contributions to overall defects differ; pyridinic and graphitic N have minimal impact on the graphene sheet as a result of comparable bond lengths of C−C (1.40 Å) and C−N (1.412 Å). However, the

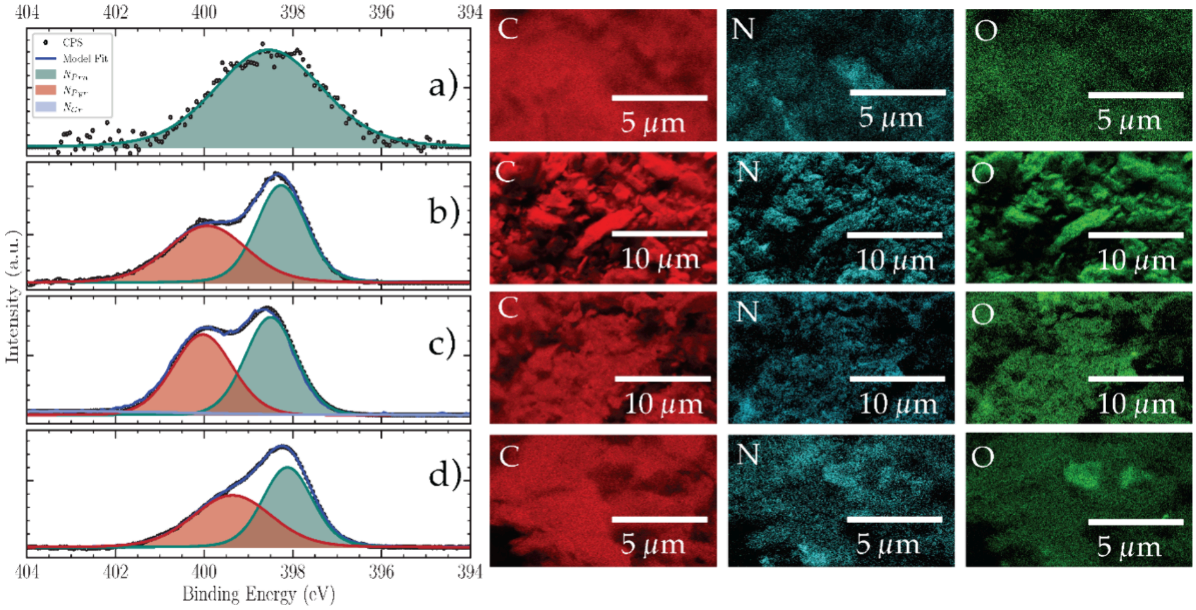

Figure 3. Spectroscopic analysis of the N-Gr samples. (a−d) XPS N 1s spectra of N-Gr 1−4, respectively, with corresponding EDS elemental mapping of C, N, and O on the surface of the graphenic microsheets.

Table 1. Chemical Compositions of N-Gr 1−4 and Their Respective Synthesis Parameters; Surface Characterizations Are Tabulated Using XPS Survey Spectra (Figure S2)

	synthesis parameters			surface characterization			bonding modality (*N*)		
	G:U (g)	temp (°C)	time (min)	C (at. %)	N (at. %)	0 (at. %)	N_{prn} (at. %)	N_{pyr} (at. %)	N_{gr} (at. %)
N-Gr 1	5:6	460	4.5	84.6	7.32	8.08	7.32		0.01
N-Gr 2	2:3	502	5	85.48	10.94	3.59	5.69	5.24	
N-Gr 3	2:3	462	5	79.47	13.59	6.94	3.74	8.75	1.10
N-Gr 4	1.7:3	496	5	70.7	26.87	2.34	13.59	13.28	

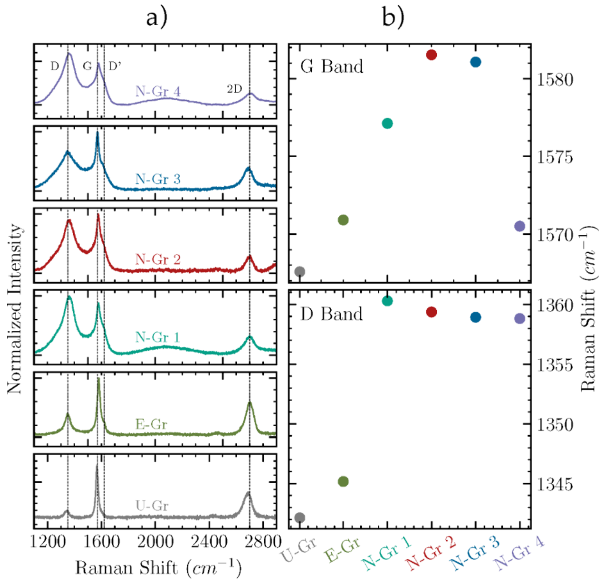

Figure 4. Raman analysis of the N-Gr samples. (a) Raman spectra obtained from GP, E-Gr, and N-Gr. (b) Blue-shift of D and G bands with respect to different levels of N-doping.

five-membered pyrrolic ring, with shorter C−N bonds (1.38 Å), introduces ring strain to the otherwise planar sheet and disrupts the graphenic structure.

It should be noted, however, that post-treatment synthesis of graphene leads to doping of the exposed surface, not the bulk. This is corroborated by our observations as well; elemental analysis was performed to ascertain the wt % of C, N, and O in our samples (Table S1), where we observed that the wt % values of *N* are less than the at. % determined via XPS, indicative of elemental doping on the surface of the graphene, not the bulk. The Brunauer−Emmett−Teller (BET) surface areas of N-Gr 1−4 were measured from the absorption/desorption nitrogen isotherms (Figure S4). It is observed that with an increase in nitrogen doping (both elemental and at. %), there is a decrease in the BET surface area, which can be attributed to a planar restacking phenomenon between graphenic sheets. This is a phenomenon also observed in reduced graphene oxide (r-GO), wherein nitrogen doping severely reduced the SSA.[48] Among other porosity parameters, the Barrett−Joyner−Halenda (BJH) average pore width measurements, which correspond to the vacancy defects on the surface of the graphenic sheet, indicate that the bulk material is largely mesoporous, with increasing width for increased N-doping. X-ray diffraction (XRD) patterns of E-Gr and N-Gr 1−4 (Figure S3) confirm the graphitic nature of the material from the characteristic single, symmetric line shape corresponding to the (002) peak at 2θ = 26.4°, indicating the presence of a single, crystalline structure. There is an increase in *d*-spacing with nitrogen doping, with the highest value being for N-Gr 3 (*d* = 3.381 Å). It should be noted that among the N-Gr samples, N-Gr 3 has the highest proportion of pyrrolic-type nitrogen doping, which introduces distortions to

https://doi.org/10.1021/acsami.4c12157

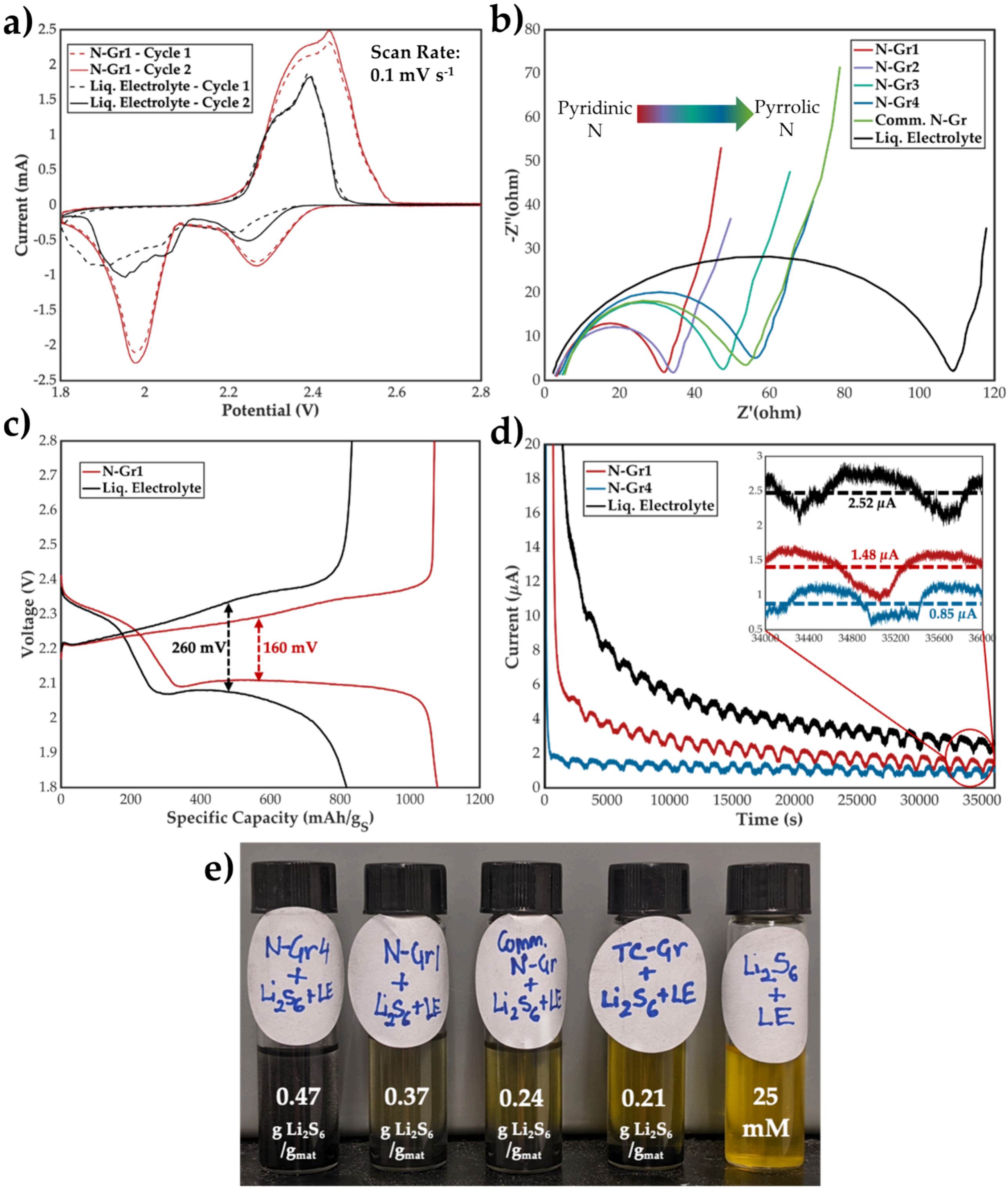

Figure 5. Electrochemical characterization of additive cells: (a) Cyclic voltammogram (cycle 1, cycle 2) of N-Gr1 + LE and LE cells at a scan rate of 0.1 mV s^{-1}. (b) Nyquist plots of additive+LE and LE-only cells before cycling. (c) Galvanostatic charge/discharge profiles at 0.2 C (post formation cycling). (d) Shuttling current measurement against time (cells set at 2.38 V during cycling at 0.2 C rate). (e) Polysulfide adsorption test for different graphenic materials (stock Li_2S_6 solution for reference).

graphenic sheets, disrupting the planar structure. Thermogravimetric analysis (TGA) was used to study the thermal stability of N-Gr (Figure S3). The minor weight loss between 30 and 120 °C can be attributed to the loss of water adsorbed to the graphene surface. A major reaction is observed at 400 °C, which can be attributed to the decomposition of the carbon skeletal structure and the loss of oxygen groups bonded to the sheet. Overall, N-Gr demonstrates excellent stability at high temperatures, with mass losses of about 20% (N-Gr 1:14%, N-Gr 2:12%, N-Gr 3:17%, N-Gr 4:20%) in the 20−1000 °C range. After the chemical characterization, the graphene

https://doi.org/10.1021/acsami.4c12157
ACS Appl. Mater. Interfaces 2024, 16, 53950−53962

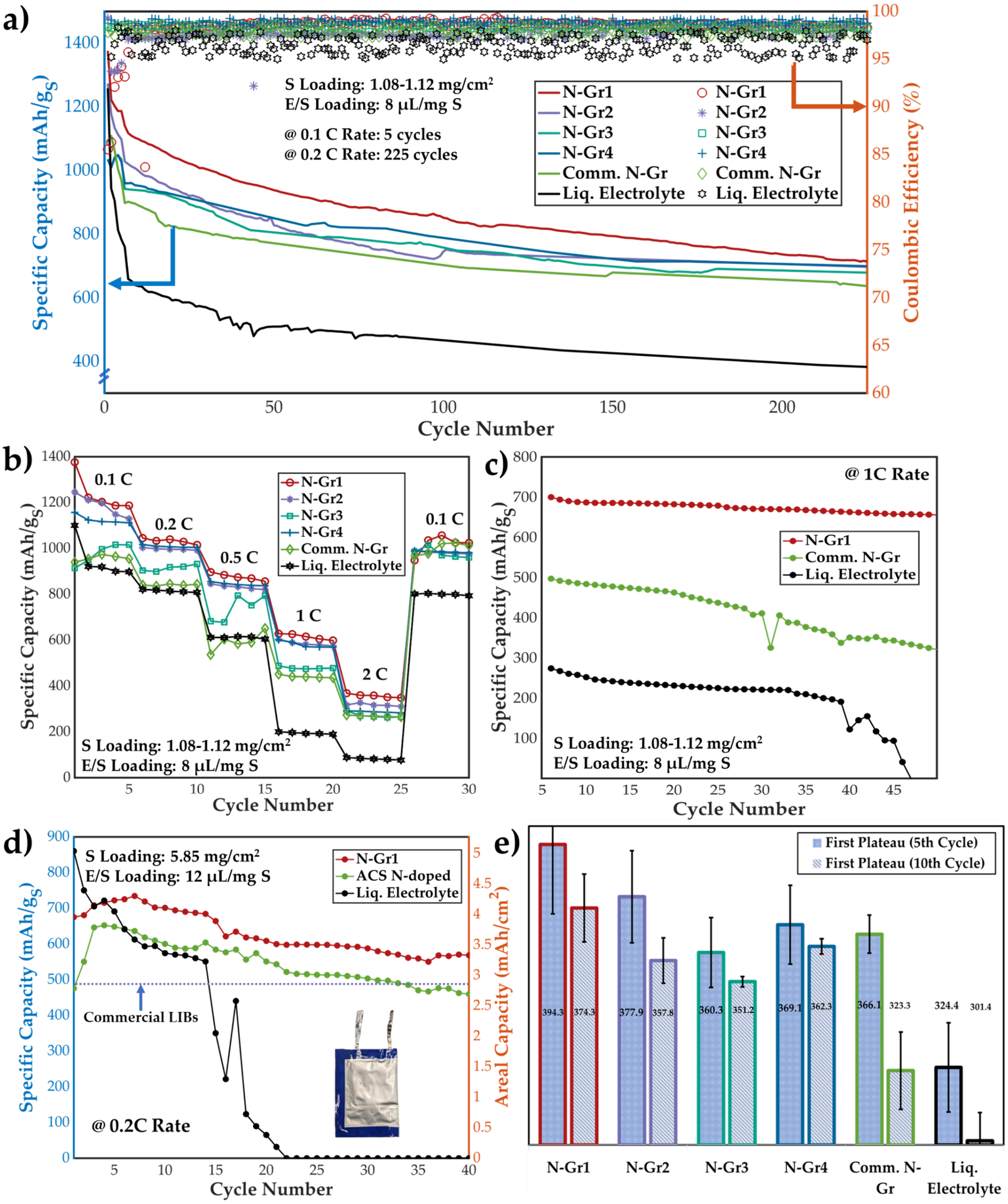

Figure 6. Electrochemical performance: (a) Galvanostatic cycling test at 0.2 C rate (post 5 formation cycles at 0.1 C). (b) Rate capability performance at different charge/discharge rates of 0.1, 0.2, 0.5, 1, and 2 C and then back to 0.1 C. (c) High-rate capability performance at 1 C rate (post 5 formation cycles at 0.1C). (d) Practical pouch cell performance at 0.2 C rate. (e) First plateau discharge capacity analysis at 0.2 C for the 5th and 10th cycle for various electrolyte combinations.

samples were utilized as electrolytic additives in the Li–S system.

Electrochemical Analysis. Extensive electrochemical characterization tests were performed to elucidate the performance of the N-doped graphenic (N-Gr) additives in the Li–S cell. Figure 5a and Figure S7 demonstrate the cyclic voltammograms (CV) for cells with N-Gr 1/LE and N-Gr 4/LE electrolyte, respectively, compared with reference LE (liquid electrolyte) cells at a scan speed of 0.1 mV s^{-1} in the potential window of 1.8–2.8 V vs Li$^+$/Li. During the cathodic scan, N-Gr 1/LE shows two reduction peaks at 2.08 and 2.3 V, corresponding to sulfur reduction to long-chain soluble polysulfides and finally to Li$_2$S. The broader oxidation peak at 2.38 V in the anodic scan corresponds to the reversible conversion of Li$_2$S to lithium polysulfides and then finally to elemental sulfur.[49]

The similar CV profile for N-Gr 1/LE, N-Gr 4/LE, and LE cells suggests the absence of parasitic side reactions from the functional groups on the N-doped graphene. The area under the peaks for the N-Gr 1/LE cells is significantly higher than that of reference LE cells, indicating superior cycling capacity due to better active material utilization and ionic conductivity, which was substantiated in subsequent tests. Unlike the LE cell, the well-overlapped cyclic voltammograms for N-Gr 1/LE cells showcase excellent cycling stability, efficiency, and high reversibility of the redox reaction in the cell.[50] Further, the higher peak current densities for N-Gr 1/LE cells suggest a much faster electron transfer rate at the electrode surface facilitated by the highly conducting graphene backbone of the additives. Additionally, a higher current density suggests that the reaction at the electrolyte/electrode is less diffusion-limited, caused by the improved Li$^+$ ionic conductivity at the interface due to the conducting "graphenic highway".[49,51]

To elucidate the impact of the nitrogen doping modality on the cell impedance and ionic conductivity, we performed electrochemical impedance tests on full cells (post formation cycling) for all the N-Gr cells compared to LE cells. Figure 5b illustrates the Nyquist plots for all of the cells. The impedance plots for the cells in the open-circuit potential states were composed of depressed semicircles in the high-frequency domain corresponding to the charge-transfer process and a sloped tail in the low-frequency domain corresponding to the semi-infinite Warburg impedance as a result of the Li$^+$ diffusion.[52] The impedance spectra were fitted to equivalent circuits (shown in Figure S6), and Table S4 displays the EIS fitting parameters for the individual spectra. A lower charge transfer resistance corresponds to increased ionic conductivity, leading to improved electrochemical reaction kinetics and hence superior cell performance (highlighted in Figure 6).

Overall, the graphene-additive cells showed a much lower charge transfer resistance compared to that of the LE cell, attributed to the improved electronic and ionic conductivity from the graphene. On further analysis of the spectra, a clear trend in the impedance of the cells emerges. It was observed that the cells with the higher pyridinic nitrogen content showed a lower impedance and charge transfer resistance at the electrolyte/electrode interface primarily caused by favorable charge- and ion-transfer processes from the graphene network and improved polysulfide mitigation due to the interaction of N dopants with LiPS. Pyrrolic doped N at defect edges causes the graphenic structure to fold due to the strained five-member cyclic structure, disrupting the electron cloud and impeding Li$^+$ ion diffusion networks.[53] DFT studies have shown improved Li$^+$ ion affinity and reduced diffusion barriers for pyridinic N compared to pyrrolic N.[54] Our experimental results closely align with these studies, as N-Gr 1, having a higher concentration of pyridinic N-doping (see Table 1 and Figure 3), exhibits a lower R_{ct} than N-Gr 4/LE cells. This reduced impedance translates to better electrochemical stability and elucidates the performance trends illustrated in Figure 6.

To better understand the impact of the electrolyte additives on the cycling performance, we studied the galvanostatic charge/discharge (GCD) profiles of the cells after formation cycling. Figure 5c and Figure S8 show the GCD profile for N-Gr 1/LE and N-Gr 4/LE cells, respectively, compared to LE cells after five 0.1 C rate charge/discharge cycles. Clearly, the additive cells show an improvement in both the first and the second plateau capacity. The improvement in the first plateau capacity, indicative of improved utilization of long-chain, soluble polysulfides, can be explained by the affinity of nitrogen toward the lithium polysulfides, which helps reduce the deleterious impact of polysulfide shuttling. This hypothesis was also validated by our DFT-based studies on the N-LiPS interaction. Further, an improvement in the second plateau capacity, an inherently kinetically mass-transport limited step, further strengthens the argument for an improvement in the Li$^+$ ion conductivity due to the graphenic additives in the electrolyte and a stable SEI layer formation. In addition, we see a marked reduction in the polarization potential, 160 and 183 mV for N-Gr 1/LE and N-Gr 4/LE cells, respectively, relative to 260 mV for reference LE cells. The excellent polysulfide immobilization causes reduced anode passivation layer formation (post-mortem results, Figure 7) and a marked improvement in ionic conductivity, leading to efficient reaction kinetics with lower energy barriers.

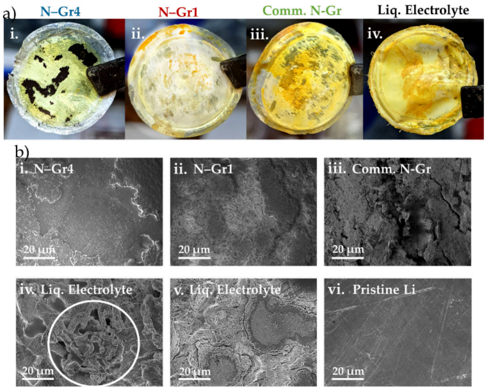

Figure 7. Post-mortem analysis: (a) Post-mortem images (cathode side) of separators after 250 cycles for (i) N-Gr 4/LE, (ii) N-Gr 1/LE, (iii) commercial N-Gr/LE, and (iv) LE only cell. (b) Scanning electron micrographs of Li anode (separator side) post 250 cycles for (i) N-Gr 4, (ii) N-Gr 1, (iii) commercial N-Gr, (iv, v) LE only cells (circled image shows dendritic formation), and (vi) pristine Li (for reference).

Next, a shuttling current measurement test was performed on the cells to quantitatively investigate the impact of N-Gr additives on suppressing PS shuttling effects. Figure 5d shows the results of the shuttling current test at 2.38 V. Studies have shown a maximum concentration of LiPS at a potential of 2.38 V, leading to the highest shuttling current while cycling.[33,55] Higher shuttling current indicates a heightened PS shuttling effect and, hence, lower cycling stability and exacerbated capacity fade, leading to a lower cell life. As shown in Figure 5d, the shuttling current for N-Gr/LE cells (0.85 μA for N-Gr 4/LE and 1.48 μA for N-Gr 1/LE cells) is much lower than that for LE cells (2.52 μA), which can be ascribed to the high polysulfide adsorption capability of the N-doped graphene significantly blocking the shuttle effect. Interestingly, N-Gr 4/LE cells showed a lower shuttle current than N-Gr 1/LE cells, suggesting that the higher nitrogen content in N-Gr 4 led to improved LiPS immobilization. The Coulombic efficiency and capacity fade over long-term cycling further substantiate this observation (Table S5 and Figure 6a). To validate this observed trend of LiPS adsorption by N-Gr, we performed a spectroscopy study to measure the polysulfide adsorption capability of the different N-doped graphene. The adsorption results were also compared with those of commercial graphene to deconvolute the physisorption effects of porous graphene. Figure 5e shows the results of the polysulfide adsorption test. The N-Gr samples show a much higher adsorption affinity to LiPS than graphene, buttressing the point that nitrogen doping on graphene improves its LiPS affinity and hence its ability to suppress polysulfide shuttling. The polysulfide adsorption of N-Gr 4 (0.47 g Li_2S_6/g_{mat}) is higher than N-Gr 1 (0.37 g Li_2S_6/g_{mat}) and commercial N-Gr (0.24 g Li_2S_6/g_{mat}) because of the higher nitrogen content, 26.9%, 7.32%, and 5.91%, respectively. Further, we see a marked difference in LiPS adsorption capacity for N-Gr 1 compared to commercial N-Gr due to the nature of N-doping. N-Gr 1 shows a purely pyridinic N-doping modality compared with commercial N-Gr, wherein the N-doping modality is primarily pyrrolic (86%) (Table S3).

Post characterization, the electrochemical performance of N-doped graphene additives in Li−S cells was evaluated. Figure 6 displays the results of electrochemical performance tests for the N-Gr additive cells. The results of the long-term cycling test for the cells are shown in Figure 6a and Table S5. The capacity is calculated based on the mass of the sulfur in the cathode. The S loading in all the cells is maintained between 1.08−1.12 mg/cm^2 to avoid trend convolution due to the complex electrode/electrolyte interactions in thick, highly loaded cathodes. Despite the high initial capacity (1258.59 mAh g_S^{-1}), without any graphenic additive, the reference LE cells suffered from a severe capacity fade. The low ionic conductivity exacerbated by the unchecked polysulfide shuttling, both leading to irreversible loss of active material, caused the capacity of LE cells to fall to almost 60% after merely five formation cycles. After 225 cycles at 0.2 C rate cycling, the final capacity was a mere 383.8 mAh g_S^{-1} (capacity retention: 50.5%), with an average Coulombic efficiency of just 95.7%. Whereas, generally, the cells with N-doped graphene additives showed a much superior cell performance with an initial capacity as high as 1376.3 mAh g_S^{-1} for N-Gr 1/LE cells, an impressive final capacity retention of almost 72.92% for N-Gr 4/LE cells (corresponding to an ultralow capacity fade rate of 0.13% per cycle), and a high average Coulombic efficiency of above 97.5%. It should be noted that the active components (cathode, anode) in all these cells were unchanged and that these remarkable gains in performance were solely due to the incorporation of N-doped graphenic species as electrolyte additives. This highlights the exceptional potential of N-functionalized graphenic species as electrolyte additives for high-performance Li−S batteries.

Additionally, familiar trends in cycling performance were observed. Pyridinic N-rich graphene species showed an impressive initial discharge capacity, primarily linked to superior Li^+ ion conductivity and improved cycling stability and efficiency. The capacity retention improved as the N doping concentration increased, ascribed to better suppression of LiPS shuttling and improved active material utilization. This is further substantiated by analyzing the first plateau capacity fade, generally assumed to be caused by inefficient reversible capacity extraction from the reduction S to long-chain LiPS due to polysulfide shuttling.[50] As shown in Figure 6b, the first plateau capacity attenuation is much lower for N-Gr 3/LE and N-Gr 4/LE as compared to N-Gr 1/LE, N-Gr 2/LE, and commercial N-Gr due to the high N-content leading to improved suppression of the polysulfide shuttle during cycling.

Next, to investigate the performance of these cells at higher current densities, the cells were subjected to a rate capability performance test, as shown in Figure 6c. It is evident that the N-doped graphene additive cells show a superior performance across all cycling current densities. However, the difference in performance is pronounced at higher C rate cycling, wherein the solid−liquid phase redox kinetics is severely mass transport limited.[56,57] N-doped graphene additive cells, owing to their superior conductivity, show vast improvement in capacity at 0.5, 1, and 2 C rates. At 0.5 C, the N-Gr 1/LE cell shows an initial capacity of 896.85 mAh g_S^{-1} compared to 612.3 mAh g_S^{-1} for the LE cell. At 1 C, the N-Gr 1/LE cell exhibits a specific capacity of 628.33 mAh g_S^{-1}, which is more than 3-fold higher than the LE cell (200.6 mAh g_S^{-1}). At 2 C capacity, the N-Gr 1/LE cell (368.6 mAh g_S^{-1}) exhibits an astonishing 4-fold higher capacity than the reference LE cell (88.4 mAh g_S^{-1}). Here, too, like in the long cycling test, we notice a similar trend in performance based on the conductivity of the pyridinic N dopants, substantiating the claim that improving the conductivity of the Li−S cells could result in significant improvement in the electrochemical performance of the cell. Finally, the N-Gr cells also show superior capacity retention at the final 0.1 C step, indicating good redox reversibility and cycling stability.

These electrochemical tests were vital in observing the trends and elucidating the impact of N-Gr species; however, it was equally important for these additives to be tested under commercially relevant practical conditions. To that end, their high-rate cycling performance capability was tested at 1 C. As shown in Figure 6d, N-Gr cells exhibit an extremely high capacity. N-Gr 1/LE and N-Gr 4/LE cells show a high initial capacity of 701.3 and 630.2 mAh g_S^{-1}, respectively, compared to 275.4 mAh g_S^{-1} for the LE cell. The additive cells also showed an impressive capacity retention of above 92.5% and an average Coulombic efficiency above 95.1%, whereas the reference LE cell suffered from low Coulombic efficiency (89.3%) and a severe capacity fade post 40 cycles owing to the unmitigated polysulfide shuttling effect and the Coulombic inefficiencies with Li anode at high-rate cycling.[58] This stabilization of the Li anode by the additives was observed experimentally in the post-mortem analysis of the cell, as shown in Figure 7. The commercial practicability of the N-Gr additive electrolyte was further explored in a lab-scale prototype single-layer pouch cell architecture. Currently, commercial traditional lithium-ion batteries show a normalized performance close to about 3 mAh/cm^2. Figure 6e shows the impressive capacities achieved by the N-Gr additive cells, peaking at 6.45 and 5.73 mAh/cm^2 for N-Gr 1/LE and N-Gr 4/LE cells, respectively. Further, the N-Gr additive cells show superior cycling stability and high Coulombic efficiencies (>95%) compared to LE cells, which, despite having a high initial capacity, suffer from severe cycling instability and low Coulombic efficiencies (~91.8%). None of the LE reference pouch cells cycled for more than 30 cycles, unlike N-Gr cells that exhibited high cycle lives beyond 150 cycles. These results further highlight the advantages of incorporating N-Gr additives toward mitigating polysulfide shuttling, improving ionic conductivity, and stabilizing the anode in Li−S cells.

Finally, to analyze the actual chemical and morphological changes in the cell caused by the additives, we carried out an *ex situ* post-mortem investigation on the separators and Li anodes extracted from the N-Gr additive and reference cells. Figure 7a shows the images of the separators extracted from the cells after 230 charging/discharging cycles. It is evident that the N-Gr additive cell separators show a significantly lower accumulation of polysulfides, ascribed to the superior polysulfide shuttling suppression capability of the N-Gr additives. Among N-Gr cells, N-Gr 4/LE separators show the least polysulfide accumulation, paralleling the PS adsorption test results. Higher nitrogen doping content causes increased polysulfide adsorption capacity, leading to superior mitigation of PS shuttling. These results are further substantiated by the Li SEM images displayed in Figure 7b. N-Gr 4/LE Li anodes show a very thin passivation layer formation with a largely pristine anode surface. N-Gr 1/LE anodes show the formation of a smooth passivation layer on the anode. This is remarkably different from the coarse passive interface layer covered with clustered mossy dendritic clumps visible on the reference LE cell anodes. This stabilization in the Li surface morphology due to the reduced anode-side Li_2S formation, resulting from suppressed PS shuttling, offers the N-Gr cells superior cycling stability, Coulombic efficiency, reduced impedance, improved ionic conductivity, and hence enhanced electrochemical performance.

Computational Analysis. Alongside experimental analysis, theoretical calculations offer a robust and intuitive framework to investigate the direct interaction between LiPS and additives. To theoretically verify and elucidate the trends and results observed experimentally, we utilized DFT and AIMD simulations to explore the influence of different nitrogen sites on the N-Gr systems toward shuttling effects.[59−61] As shown in Figure 8, the adsorption energies of Li_2S_4, Li_2S_6, and Li_2S_8 were calculated over the pyridinic and pyrrolic N sites doped on the graphene surface. The initial structures of Li_2S_4, Li_2S_6, and Li_2S_8 were adopted from the previous theoretical studies on the Li−S systems.[62−64]

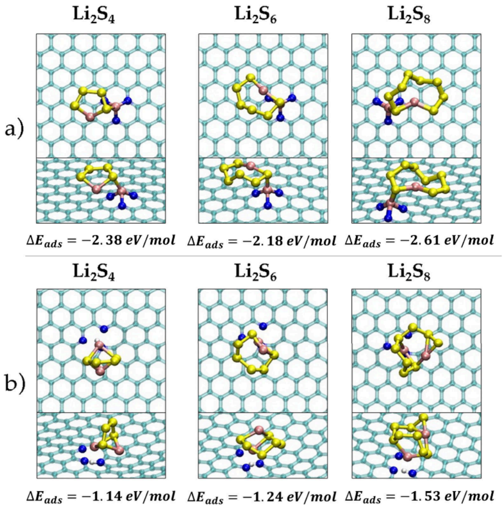

Figure 8. DFT-optimized configurations of Li_2S_4, Li_2S_6, and Li_2S_8 adsorbed on the (a) pyridinic and (b) pyrrolic nitrogen site on the graphene surface. The green, white, blue, ochre, and yellow balls in the DFT models represent carbon, hydrogen, nitrogen, lithium, and sulfur atoms, respectively. Bare N-doped graphene surfaces can also be found in Figure S12.

We found that the adsorption energy of LiPS is significantly higher (≫1.00 eV/molecule) on the pyridinic N sites compared to the pyrrolic N sites, regardless of the type of LiPS. LiPS species are more strongly anchored at the pyridinic N sites relative to pyrrolic N sites, as reflected by the Li−N bond distance (1.9 Å for pyridinic N versus 2.2 Å for pyrrolic N). Such a trend in anchoring effects was also seen with the performance of the N-doped graphene model for Li-ion battery applications.[54] On analysis of the charge distribution to understand the true nature of the interaction, we observe that a large charge accumulation is seen between Li and N sites on the graphene surface, as shown by the differential charge density plots of Li_2S_4, Li_2S_6, and Li_2S_8 over the N-doped graphene surface in Figure S13. In fact, larger charge accumulation is observed for the Li atom of LiPS directly interacting with pyridinic N sites compared to pyrrolic N sites, as also described in Table S6, further indicating a stronger interaction of pyridinic N sites with LiPS through the Li atom. Overall, our theoretical results confirm that the pyridinic N site is more effective at minimizing shuttling effects compared to the pyrrolic N site, agreeing with the experimental findings on improved capacity retention and cycling stability for pyridinic N-Gr additives.

■ CONCLUSION

In summary, we successfully report a facile, scalable, and green approach to fabricating highly functionalized, modality-tunable, N-doped graphene for additives in ether-based liquid electrolytes for Li−S cells. Thermally annealing the TCR graphene in urea ensures the cost-effectiveness and scalability of the N-Gr production while maintaining environmental friendliness, as it foregoes the use of any organic solvents in the entire process. The fabricated N-Gr was used as a low-mass-loading additive in the ether-based liquid electrolyte Li−S cells. This study reports the beneficial role of highly doped N-Gr in significantly improving the electrochemical performance of Li−S systems via a series of polysulfide adsorption experiments, electrochemical characterization and performance tests, and cell post-mortem analysis. Our results highlighted several key electrochemical performance trends associated with changing the N-doping concentration and modality on graphene. With increasing pyridinic N-dopant content on graphene, the cell showed enhanced ionic conductivity, improved high-rate kinetics, and reduced polarization in the cell, explained by better Li^+ affinity with pyridinic N dopants. Overall, N-Gr with a higher pyridinic N-doping content showed improved ionic conductivity than those with high pyrrolic N-doping. Further, LiPS adsorption studies and cell post-mortem analysis revealed that higher N-doping concentration for the additives was positively correlated to better LiPS anchoring, showing better active material utilization, lower capacity fade, and improved cycling stability. This is also corroborated by our DFT and AIMD studies, which demonstrate the increased affinity of LiPS to pyridinic nitrogen-decorated graphene. This study, to the best of our knowledge, incorporates the first attempt to integrate both experimental and computational analysis to truly elucidate the electrochemical performance of N-doped graphenic species in the Li−S system. We strongly believe that our study highlights the exceptional potential of N-Gr as an efficient, commercially viable electrolytic additive for traditional Li−S batteries.

■ MATERIALS AND EXPERIMENTAL METHODS

Materials. 1-Methyl-2-pyrrolidone (NMP), poly(vinylidene fluoride) (PVDF, average MW ∼ 534000), lithium sulfide (Li_2S, 99.98% trace metal basis), 1,2-dimethoxyethane (DME), 1,3-dioxolane (DOL), and bis(trifluoromethane)lithium salt (LiTFSI, 99.95%) were purchased from Sigma-Aldrich. Timical Super C65 was purchased from MTI Corp. Sulfur powder (sublimed, 100 mesh, 99.5%) and lithium metal (0.75 mm thickness) were purchased from Alfa Aesar. Ketjen Black EC-600JD porous carbon was purchased from Akzo Nobel Functional Chemicals LLC. Natural graphite powder was purchased from Asbury Carbon (50 μm, Lot 21646, Container 23). Urea used in the doping process was sourced from Sigma-Aldrich (CAS: 57-13-6). These materials were used without any further processing. The commercial carbon materials for electrolyte additives used in this study are as follows: (1) single-layer graphene (ACS Material); (2) N-doped graphene (ACS Material). All the carbon materials were used after drying in a vacuum oven at 600 °C overnight.

Few-Layered Graphene and N-Doped Graphene Fabrication. Facile, low-cost, aqueous-based graphene was manufactured in-house using a patented Taylor−Couette reactor that employs outer cylinder rotation with a stationary inner cylinder, along with axial-driven flow that recirculates the fluid, creating a semicontinuous exfoliation process. Processing parameters for the reactor were as follows: gap between inner and outer cylinder (127−1270 μm), shear rates (5000−13000 s^{-1}), axial flow rate (100−1000 mL/min), processing volume (150−600 mL), and processing time (0.5−3 h). After exfoliation, solutions were washed with DI water and centrifuged to remove any unexfoliated graphite particles. The doping process was performed in a 100 mL stainless steel autoclave reactor. Exfoliated graphite and commercial urea were ball milled (30 Hz, 20 min) to ensure homogeneity. The mixture was then placed in the autoclave reactor, which was subsequently purged using Ar gas, following which a constant Ar blanket was maintained for the duration of the reaction. The reactor was then heated to 350−500 °C over the course of 1 h and held at the reaction temperature for 56.5 min. The reaction mixture was air-quenched by immediate removal of the sample from the reactor, and the unreacted urea was removed by washing with DI water and subsequent drying to obtain pristine N-Gr samples.

Materials Characterization. Surface morphology and EDS elemental mapping of N-Gr and E-Gr powders were studied by SEM (Zeiss Gemini 500 SEM, ETH = 3−5 keV, WD = 5−9 mm). Graphene particle width and lateral dimensions were confirmed using STEM (Zeiss Gemini 500 STEM, ETH = 30 keV, WD = 2.5 mm) by imaging drop-cast graphene solution on a 400 mesh Cu grid (lacey carbon support). The thermal stability of N-Gr was studied using thermogravimetric analysis (TA Instruments 5500 TGA, 100 °C min^{-1} ramp from 30−1000 °C, N_2 atmosphere). Nitrogen doping was analyzed using X-ray photoelectron spectroscopy (Scienta Omicron ESCA-2SR spectrometer with operating pressure ca. 10^{-9} Torr, monochromatic Al Kα X-rays at 1486.6 eV) with a 1.1 mm diameter analysis spot. Photoelectrons were collected at a 90° emission angle with a source-to-analyzer angle of 54.7°. A hemispherical analyzer determined electron kinetic energy using a pass energy of 200 eV for survey scans and 20 eV for high-resolution scans. A flood gun was used for charge neutralization of nonconductive samples; all samples were charge corrected using graphitic carbon binding energy (284.8 eV). Nitrogen doping was further quantified (wt %) in triplicate using a CE-440 elemental analyzer (Exeter Analytical). Raman spectra from 5 different areas of graphene powders on a glass slide were obtained by Raman spectroscopy (Renishaw InVia confocal Raman microscope, 532 nm with ULF). X-ray diffraction (XRD) patterns of the graphene samples were determined by a D8 Advance ECO powder diffractometer (Bruker Corporation) using a high-brilliance 1 kW X-ray source. Prior to BET analysis, the samples were degassed under a vacuum (10 mmHg) at 120 °C for 2 h. Subsequently, the BET specific surface area was determined on an ASAP 2020 Micromeritics instrument with N_2 gas adsorption at 77 K.

Electrolyte Fabrication. The liquid electrolyte was fabricated in an Ar-filled glovebox (MBraun MB 150B-G) maintained at moisture and oxygen levels below 0.1 ppm. The liquid electrolyte was fabricated with 1 M lithium bis(trifluoromethanesulfonyl) (LiTFSI) and 1 wt % lithium nitrate ($LiNO_3$) dissolved in 1,2-dimethoxyethane and 1,3-dioxolane (1:1 by volume). The chemicals were mixed and stirred at 1500 rpm overnight. The additive loading was maintained between 0.25% w/w of liquid electrolyte solution. The mixture was then ultrasonicated for 90 min and thereafter used immediately.

Cathode Preparation. Mesoporous carbon (C) sulfur (S) cathodes were fabricated as cathodes for the Li−S cells. Sulfur and Ketjen Black (KB) were homogeneously mixed at a mass ratio of 8:2 using a mortar and pestle. The mixture was sealed and heated to 155 °C for 12 h to melt-infiltrate the sulfur in the mesoporous KB host. The S-infiltrated mixture was mixed with conductive Super C65 using a mortar and pestle. Next, 5% w/w PVDF solution in NMP was added to the powder precursor, and the mixture ball was milled for 4 h (total, 10 min intervals to prevent overheating) using a Retsch Mixer Mill MM 400 in a hardened stainless-steel jar (50 mL capacity) with 25 3 mm stainless steel beads. NMP was added to the mixture periodically to transform the mix into a castable slurry. The final composition of the slurry was 70% w/w S/KB mixture, 20% w/w Super C65, and 10% w/w PVDF with 12−17 mL of NMP added. The slurry was then cast onto a battery-grade Al foil current collector using an MSK-AFA-III automatic thick film coater, followed by a 2-step drying process: drying at room temperature for 12 h and then drying at 60 °C for 6 h in a forced convection dryer. The cathodes were stored in a desiccator set at humidity <10%. The cathodes were fabricated at 250−400 μm thickness to achieve the corresponding mass loading, 1 mg/cm^2 for coin cells and 5.85 mg/cm^2 for pouch cells. The dried casted films were punched into 15 mm diameter discs for CR2032 cells and 2 × 3 cm^2 for pouch cells. All cell performance comparisons were made between cells fabricated from the same sheet of the cathode to deconvolute the impact of active material and ensure differences in electrochemical performance were solely due to differences in electrolyte additives.

Cell Assembly. CR2032-type coin cells and pouch cells were used to evaluate and elucidate the electrochemical performances of graphene-based electrolyte additives in the Li−S cell. The coin cells were assembled in the Ar-filled glovebox (MBraun MB 150B-G). Lithium metal was used as the anode, and the additive-loaded liquid electrolyte was employed as the electrolyte with an electrolyte-to-sulfur (E/S) ratio of 15 $\mu L/mg_S{}^{-1}$, and the C−S composite film was employed as the cathode. A commercial microporous polypropylene membrane (Celgard 2400) was used as the separator. For pouch cells, the slurry-casted cathodes were cut into 2 × 3 cm^2 rectangles. Aluminum tabs (MTI Corp, PLIB-ATC4) were welded onto cathodes using a Branson 2000Xd ultrasonic welder to allow electric contact outside the insulating pouch. Similarly, nickel tabs (MTI Corp, PLIB-NTA4) were welded onto 1 × 0.5 cm^2 copper-mesh current collectors, which were then pressed onto 2 × 3 cm^2 lithium foil of 0.75 mm thickness in an argon-filled glovebox. Then, in the glovebox, the cathode, Celgard 2400 separator, and lithium anode were stacked and fixed onto insulative hot-seal aluminum foils with double-sided tape (3M 200MP acrylic). The electrolyte was injected into the stack, and the aluminum foils were vacuum-sealed on four sides to make a pouch. (A gas pouch was created to collect gas formation during formation cycling, though there was no visible gas collection.)

Electrochemical Measurements. The galvanostatic charge−discharge cycling test was performed between 1.8 and 2.8 V using a Landt CT3002A battery test system. All cells were rested for 3 h prior to initiating any electrochemical testing. The testing protocol was as follows: (i) five formation cycles at 0.1 C, followed by (ii) 225 cycles (or otherwise stated) at a 0.2 C rate. For rate capability testing, the cells were charged/discharged between 1.8 and 2.8 V vs Li^+/Li at 0.1, 0.2, 0.5, 1, and 2 C and back to 0.1 C for five cycles each. Capacity retentions were calculated against the first cycle after the formation steps. A BioLogic SP-150 potentiostat was used for cyclic voltammetry (CV) and electrochemical impedance spectrometry (EIS). The CV measurements were carried out at a scan rate of 0.02 mV s^{-1} within 1.8−2.8 V. EIS analyses were carried out in a frequency range of 100 kHz to 0.1 Hz. The shuttling current test was conducted by running a cell for 2 complete charge/discharge cycles at 0.1 C; then the cell was held at 2.38 V for 36000 s (10 h), and the current response was measured and plotted. The measured current at steady state measures the shuttling current in the cell. All cycling and electrochemical measurements were conducted at 25 °C. For the polysulfide adsorption test, first, an adsorption curve for various Li_2S_6 concentrations (Figure S9) was prepared by fabricating stock solutions of various concentrations of Li_2S_6 (prepared by mixing stoichiometric quantities of Li_2S and S in DOL/DME and heating to 70 °C for 24 h) and measuring their absorbance at 430 nm using a UV−vis spectrophotometer and then fitting a concentration calibration curve based on the Beer−Lambert law. Then, 25 mg of graphenic material is added to 10 mL of 25 mM solution vials of Li_2S_6 in DOL/DOE (1:1 v/v). First, the solution is stirred mildly for 3 h and then left untouched for 72 h. After 72 h, the solution is filtered, and the concentration of the supernatant solution is measured postdilution using the UV−vis spectrophotometer and the concentration calibration curve.

Computational Methodology. Periodic DFT calculations were performed using the Perdew−Burke−Ernzerhof (PBE)[65] form of the generalized gradient approximation (GGA), as implemented in the CP2K software package.[66] The Goedecker−Teter−Hutter (GTH) pseudopotentials[67] are chosen to treat core electrons, and the valence electron states are computed with the double-ζ Gaussian basis sets.[68] A 400 Ry cutoff was used to describe the electrostatic terms. The Γ-point is sufficient for sampling the Brillouin zone due to the large size of the supercell. Long-range dispersion (van der Waals) corrections are applied using the Grimmes DFT-D2 approach.[69] The lattice parameters of graphene basal plane, consisting of 400 atoms, are chosen as $a = 29.47$ Å, $b = 34.00$ Å, and $c = 32.00$ Å ($\alpha = \beta = \gamma = 90°$) with a vacuum space of 32 Å in the z-direction. The geometry optimization of the pristine graphene surface was initially performed using the BFGS algorithm. DFT-based AIMD simulations were also carried out in the canonical NVT ensembles using a 1.0 fs time step and a Nosé−Hoover chain thermostat at 298.15 K. To obtain the dynamic features of LiPS interacting with the N-doped graphene surface, we select the following systems: (i) a pristine graphene basal plane, (ii) pyrrolic and pyridinic-type N atoms doped on the graphene basal plane, and (iii) LiPS (Li_2S_4, Li_2S_6, and Li_2S_8) adsorbed on the N-doped graphene surface. Well-equilibrated trajectories of at least 5 ps were sampled for each system to ensure reliable statistical properties. Subsequently, we performed computational annealing on several structures from the AIMD trajectories to 0 K and further optimized them at 0 K, so that the representative structures of adsorbed LiPS can be obtained on the N-doped graphene surface. Furthermore, the adsorption energy of LiPS (eV/molecule) on the N-doped graphene surface (ΔE_{ads}) is calculated as follows:

$$\Delta E_{ads} = E_{tot,ads} - E_{surf,grap} - E_{LiPS,gas}$$

where $E_{tot,ads}$ represents the energy of adsorbed LiPS on the N-doped graphene surface, $E_{surf,grap}$ is the energy of pristine N-doped graphene surface before adsorption, and $E_{LiPS,gas}$ defines the energy of gas-phase LiPS. To further understand the charge profile of LiPS adsorbed on the N-doped graphene surface, the differential charge density plot $\Delta\rho_{diff}$ was obtained by

$$\Delta\rho_{diff} = \rho_{tot,ads} - \rho_{surf,grap} - \rho_{LiPS,gas}$$

where $\rho_{tot,ads}$ represents the charge density of adsorbed LiPS on the N-doped graphene surface, $\rho_{surf,grap}$ is the charge density of pristine N-doped graphene surface before adsorption, and $\rho_{LiPS,gas}$ is the charge density of gas-phase LiPS. Bader charge analysis[70] was also used to evaluate a charge transfer between adsorbed LiPS and N-doped graphene surface.

ASSOCIATED CONTENT

Supporting Information

The Supporting Information is available free of charge at https://pubs.acs.org/doi/10.1021/acsami.4c12157.

Figures S1−S13 and Tables S1−S8 (PDF)

AUTHOR INFORMATION

Corresponding Author

Yong Lak Joo − *Robert Fredrick Smith School of Chemical and Biomolecular Engineering, Cornell University, Ithaca, New York 14853, United States;* orcid.org/0000-0002-4646-1625; Phone: +1 607 255 8591; Email: ylj2@cornell.edu

Authors

Vaidik R. Shah − *Robert Fredrick Smith School of Chemical and Biomolecular Engineering, Cornell University, Ithaca, New York 14853, United States*

Ritwick Sinha − *Robert Fredrick Smith School of Chemical and Biomolecular Engineering, Cornell University, Ithaca, New York 14853, United States;* orcid.org/0000-0002-9732-935X

Walter J. Cesarski − *Department of Chemistry and Life Science, United States Military Academy, West Point, New York 10996, United States*

Xiaosi Gao − *Robert Fredrick Smith School of Chemical and Biomolecular Engineering, Cornell University, Ithaca, New York 14853, United States;* orcid.org/0000-0002-3018-9508

Simuck F. Yuk − *Department of Chemistry and Life Science, United States Military Academy, West Point, New York 10996, United States;* orcid.org/0000-0003-1355-4400

Complete contact information is available at: https://pubs.acs.org/10.1021/acsami.4c12157

Author Contributions

V.R.S. and R.S. contributed equally to the project. Y.L.J. and V.R.S. conceived the project. R.S. designed and executed N-Gr and FLG fabrication process and performed subsequent chemical characterization. V.R.S. designed and performed the electrochemical experiments and cell tests. X.G. fabricated pouch cells. W.J.C. and S.F.Y. performed the computational studies. All authors analyzed the data and discussed the experimental plans. V.R.S. and R.S. drafted the manuscript, and all authors were involved in its revision. Y.L.J. supervised the whole project.

Notes

The authors declare no competing financial interest.

ACKNOWLEDGMENTS

The authors acknowledge Dr. Nicholas Schulman and Dharani Prasad for their help in fabricating FLG, N-Gr, and elemental analysis of the N-Gr samples. The authors also acknowledge Iftekar Ahmed and Prithwiraj De for their assistance with the illustrations. This work was partially supported by Saudi Aramco and used the Cornell Center of Materials Research Shared Facilities, which are supported through the NSF MRSEC program (DMR-1719875). Computational Resources were provided by user proposals at the National Energy Research Scientific Computing Center (NERSC) located at Lawrence Berkley National Laboratory (LBNL). The opinions expressed herein are those of the authors and not necessarily representative of those of the Department of the Army, Department of Defense (DoD), or U.S. Government.

REFERENCES

(1) Manthiram, A.; Fu, Y.; Su, Y. S. Challenges and Prospects of Lithium-Sulfur Batteries. *Acc. Chem. Res.* **2013**, *46* (5), 1125−1134.

(2) Shah, V. R. Tailoring Crosslinked Gelled Electrolyte and Probing Its Synergistic Performance with Polymer-Ceramic Hybrid Separators for High Energy Density Lithium-Sulfur Battery Systems. **2021**. DOI: 10.7298/9BNZ-T457.

(3) Seo, S.-D.; Park, D.; Park, S.; Kim, D.-W. "Brain-Coral-Like" Mesoporous Hollow CoS2@N-Doped Graphitic Carbon Nanoshells as Efficient Sulfur Reservoirs for Lithium-Sulfur Batteries. *Adv. Funct. Mater.* **2019**, *29* (38), 1903712.

(4) Ye, Y.; Wu, F.; Liu, Y.; Zhao, T.; Qian, J.; Xing, Y.; Li, W.; Huang, J.; Li, L.; Huang, Q.; Bai, X.; Chen, R. Toward Practical High-Energy Batteries: A Modular-Assembled Oval-Like Carbon Microstructure for Thick Sulfur Electrodes. *Adv. Mater.* **2017**, *29* (48), 1700598.

(5) Lin, H.; Zhang, S.; Zhang, T.; Cao, S.; Ye, H.; Yao, Q.; Zheng, G. W.; Lee, J. Y. A Cathode-Integrated Sulfur-Deficient Co9S8 Catalytic Interlayer for the Reutilization of Lost Polysulfides in LithiumSulfur Batteries. *ACS Nano* **2019**, *13* (6), 7073−7082.

(6) Lin, Q.; Ding, B.; Chen, S.; Li, P.; Li, Z.; Shi, Y.; Dou, H.; Zhang, X. Atomic Layer Deposition of Single Atomic Cobalt as a Catalytic Interlayer for Lithium-sulfur Batteries. *ACS Appl. Energy Mater.* **2020**, *3* (11), 11206−11212.

(7) Yuan, Z.; Peng, H. J.; Hou, T. Z.; Huang, J. Q.; Chen, C. M.; Wang, D. W.; Cheng, X. B.; Wei, F.; Zhang, Q. Powering Lithium-Sulfur Battery Performance by Propelling Polysulfide Redox at Sulfiphilic Hosts. *Nano Lett.* **2016**, *16* (1), 519−527.

(8) Gao, X.; Zheng, C.; Shao, Y.; Shah, V. R.; Jin, S.; Suntivich, J.; Joo, Y. L. Lithium Iron Phosphate Enhances the Performance of High-Areal-Capacity Sulfur Composite Cathodes. *ACS Appl. Mater. Interfaces* **2023**, *15* (15), 19011−19020.

(9) Fan, Z.; Ding, B.; Li, Z.; Hu, B.; Xu, C.; Xu, C.; Dou, H.; Zhang, X. Long-Cycling All-Solid-State Batteries Achieved by 2D Interface between Prelithiated Aluminum Foil Anode and Sulfide Electrolyte. *Small* **2022**, *18* (44), 2204037.

(10) Zhao, G.; Suzuki, K.; Yonemura, M.; Hirayama, M.; Kanno, R. Enhancing Fast Lithium Ion Conduction in Li4GeO4-Li3PO4 Solid Electrolytes. *ACS Appl. Energy Mater.* **2019**, *2* (9), 6608−6615.

(11) Yu, X.; Wu, H.; Koo, J. H.; Manthiram, A. Tailoring the Pore Size of a Polypropylene Separator with a Polymer Having Intrinsic Nanoporosity for Suppressing the Polysulfide Shuttle in Lithium-Sulfur Batteries. *Adv. Energy Mater.* **2020**, *10* (1), 1902872.

(12) Deng, C.; Wang, Z.; Wang, S.; Yu, J.; Martin, D. J.; Nanjundan, A. K.; Yamauchi, Y. Double-Layered Modified Separators as Shuttle Suppressing Interlayers for Lithium-Sulfur Batteries. *ACS Appl. Mater. Interfaces* **2019**, *11* (1), 541−549.

(13) Chung, S. H.; Manthiram, A. High-Performance Li-S Batteries with an Ultra-Lightweight MWCNT-Coated Separator. *J. Phys. Chem. Lett.* **2014**, *5* (11), 1978−1983.

(14) Zhou, G.; Li, L.; Wang, D. W.; Shan, X. Y.; Pei, S.; Li, F.; Cheng, H. M. A Flexible Sulfur-Graphene-Polypropylene Separator Integrated Electrode for Advanced Li-S Batteries. *Adv. Mater.* **2015**, *27* (4), 641−647.

(15) Bai, S.; Liu, X.; Zhu, K.; Wu, S.; Zhou, H. Metal-Organic Framework-Based Separator for Lithium-Sulfur Batteries. *Nature Energy* **2016**, *1* (7), 1−6.

(16) Bai, S.; Zhu, K.; Wu, S.; Wang, Y.; Yi, J.; Ishida, M.; Zhou, H. A Long-Life Lithium-Sulphur Battery by Integrating Zinc-Organic Framework Based Separator. *J. Mater. Chem. A Mater.* **2016**, *4* (43), 16812−16817.

(17) Hao, J.; Pan, Y.; Chen, W.; Zhu, X.; Zhou, Y.; Chou, S. Improving the Li-S Battery Performance by Applying a Combined Interface Engineering Approach on the Li2S Cathode. *J. Mater. Chem. A Mater.* **2019**, *7* (48), 27247−27255.

(18) Shah, V.; Joo, Y. L. Incorporation of Functionalized Graphene and Its Derivates into Electrolyte: A Facile Approach to Improve the Electrochemical Performance of Lithium-Sulfur Batteries. *ECS Meeting Abstracts* **2022**, *MA2022-01* (1), 82.

(19) Shah, V.; Joo, Y. L. Incorporating Heteroatom-Doped Graphene in Electrolyte for High-Performance Lithium-Sulfur Batteries. *ECS Meeting Abstracts* **2022**, *MA2022-02* (8), 656.

(20) Reddy, A. L. M.; Srivastava, A.; Gowda, S. R.; Gullapalli, H.; Dubey, M.; Ajayan, P. M. Synthesis of Nitrogen-Doped Graphene Films for Lithium Battery Application. *ACS Nano* **2010**, *4* (11), 6337−6342.

(21) Balandin, A. A.; Ghosh, S.; Bao, W.; Calizo, I.; Teweldebrhan, D.; Miao, F.; Lau, C. N. Superior Thermal Conductivity of Single-Layer Graphene. *Nano Lett.* **2008**, *8* (3), 902−907.

(22) Wang, X.; Ding, Y.; Lu, H.; Chen, F.; Zhang, N.; Ma, M. Chemoselective Solution Synthesis of Pyrazolic-Structure-Rich Nitrogen-Doped Graphene for Supercapacitors and Electrocatalysis. *Chem. Eng. J.* **2018**, *347*, 754−762.

(23) Usachov, D.; Vilkov, O.; Grüneis, A.; Haberer, D.; Fedorov, A.; Adamchuk, V. K.; Preobrajenski, A. B.; Dudin, P.; Barinov, A.; Oehzelt, M.; Laubschat, C.; Vyalikh, D. V. Nitrogen-Doped Graphene: Efficient Growth, Structure, and Electronic Properties. *Nano Lett.* **2011**, *11* (12), 5401−5407.

(24) Qu, L.; Liu, Y.; Baek, J. B.; Dai, L. Nitrogen-Doped Graphene as Efficient Metal-Free Electrocatalyst for Oxygen Reduction in Fuel Cells. *ACS Nano* **2010**, *4* (3), 1321−1326.

(25) Thomsen, C.; Reich, S. Double Resonant Raman Scattering in Graphite. *Phys. Rev. Lett.* **2000**, *85* (24), 5214.

(26) Chen, J.; Han, Y.; Kong, X.; Deng, X.; Park, H. J.; Guo, Y.; Jin, S.; Qi, Z.; Lee, Z.; Qiao, Z.; Ruoff, R. S.; Ji, H. The Origin of Improved Electrical Double-Layer Capacitance by Inclusion of Topological Defects and Dopants in Graphene for Supercapacitors. *Angew. Chem., Int. Ed.* **2016**, *55* (44), 13822−13827.

(27) Hu, H.; Chen, N.; Teng, H.; Yu, R.; Qu, Y.; Sun, J.; Xue, M.; Hu, D.; Wu, B.; Li, C.; Chen, J.; Liu, M.; Sun, Z.; Liu, Y.; Li, P.; Fan, S.; García de Abajo, F. J.; Dai, Q. Doping-Driven Topological Polaritons in Graphene/α-MoO3 Heterostructures. *Nature Nanotechnology* **2022**, *17* (9), 940−946.

(28) Yi, G. S.; Sim, E. S.; Chung, Y. C. Effect of Lithium-Trapping on Nitrogen-Doped Graphene as an Anchoring Material for Lithium-Sulfur Batteries: A Density Functional Theory Study. *Phys. Chem. Chem. Phys.* **2017**, *19* (41), 28189−28194.

(29) Huang, M.; Mi, K.; Zhang, J.; Liu, H.; Yu, T.; Yuan, A.; Kong, Q.; Xiong, S. MOF-Derived Bi-Metal Embedded N-Doped Carbon Polyhedral Nanocages with Enhanced Lithium Storage. *J. Mater. Chem. A Mater.* **2017**, *5* (1), 266−274.

(30) Pang, Q.; Nazar, L. F. Long-Life and High-Areal-Capacity Li-S Batteries Enabled by a Light-Weight Polar Host with Intrinsic Polysulfide Adsorption. *ACS Nano* **2016**, *10* (4), 4111−4118.

(31) Zhang, R.; Chen, X. R.; Chen, X.; Cheng, X. B.; Zhang, X. Q.; Yan, C.; Zhang, Q. Lithiophilic Sites in Doped Graphene Guide Uniform Lithium Nucleation for Dendrite-Free Lithium Metal Anodes. *Angew. Chem., Int. Ed.* **2017**, *56* (27), 7764−7768.

(32) Wang, C.; Su, K.; Wan, W.; Guo, H.; Zhou, H.; Chen, J.; Zhang, X.; Huang, Y. High Sulfur Loading Composite Wrapped by 3D Nitrogen-Doped Graphene as a Cathode Material for Lithium-Sulfur Batteries. *J. Mater. Chem. A Mater.* **2014**, *2* (14), 5018−5023.

(33) Fu, Y.; Wu, Z.; Yuan, Y.; Chen, P.; Yu, L.; Yuan, L.; Han, Q.; Lan, Y.; Bai, W.; Kan, E.; Huang, C.; Ouyang, X.; Wang, X.; Zhu, J.; Lu, J. Switchable Encapsulation of Polysulfides in the Transition between Sulfur and Lithium Sulfide. *Nature Communications* **2020**, *11* (1), 1−10.

(34) Wang, H.; Maiyalagan, T.; Wang, X. Review on Recent Progress in Nitrogen-Doped Graphene: Synthesis, Characterization, and Its Potential Applications. *ACS Catal.* **2012**, *2* (5), 781−794.

(35) Zhang, C.; Fu, L.; Liu, N.; Liu, M.; Wang, Y.; Liu, Z. Synthesis of Nitrogen-Doped Graphene Using Embedded Carbon and Nitrogen Sources. *Adv. Mater.* **2011**, *23* (8), 1020−1024.

(36) Pham, T. V.; Kim, J. G.; Jung, J. Y.; Kim, J. H.; Cho, H.; Seo, T. H.; Lee, H.; Kim, N. D.; Kim, M. J. High Areal Capacitance of N-Doped Graphene Synthesized by Arc Discharge. *Adv. Funct. Mater.* **2019**, *29* (48), 1905511.

(37) Rybin, M.; Pereyaslavtsev, A.; Vasilieva, T.; Myasnikov, V.; Sokolov, I.; Pavlova, A.; Obraztsova, E.; Khomich, A.; Ralchenko, V.; Obraztsova, E. Efficient Nitrogen Doping of Graphene by Plasma Treatment. *Carbon N Y* **2016**, *96*, 196−202.

(38) Singh, A. K.; Basavaraju, K. C.; Sharma, S.; Jang, S.; Park, C. P.; Kim, D. P. Eco-Efficient Preparation of a N-Doped Graphene Equivalent and Its Application to Metal Free Selective Oxidation Reaction. *Green Chem.* **2014**, *16* (6), 3024−3030.

(39) Du, M.; Sun, J.; Chang, J.; Yang, F.; Shi, L.; Gao, L. Synthesis of Nitrogen-Doped Reduced Graphene Oxide Directly from Nitrogen-Doped Graphene Oxide as a High-Performance Lithium Ion Battery Anode. *RSC Adv.* **2014**, *4* (80), 42412−42417.

(40) Figueras, M.; Villar-Garcia, I. J.; Vines, F.; Sousa, C.; De La Pena O'Shea, V. A.; Illas, F. Correcting Flaws in the Assignment of Nitrogen Chemical Environments in N-Doped Graphene. *J. Phys. Chem. C* **2019**, *123* (17), 11319−11327.

(41) Alamer, M.; Zamani, S.; Fok, K.; Satish, A.; Lim, A. R.; Joo, Y. L. Facile Production of Graphenic Microsheets and Their Assembly via Water-Based, Surfactant-Aided Mechanical Deformations. *ACS Appl. Mater. Interfaces* **2020**, *12* (7), 8944−8951.

(42) Paton, K. R.; Varrla, E.; Backes, C.; Smith, R. J.; Khan, U.; O'Neill, A.; Boland, C.; Lotya, M.; Istrate, O. M.; King, P.; Higgins, T.; Barwich, S.; May, P.; Puczkarski, P.; Ahmed, I.; Moebius, M.; Pettersson, H.; Long, E.; Coelho, J.; O'Brien, S. E.; McGuire, E. K.; Sanchez, B. M.; Duesberg, G. S.; McEvoy, N.; Pennycook, T. J.; Downing, C.; Crossley, A.; Nicolosi, V.; Coleman, J. N. Scalable Production of Large Quantities of Defect-Free Few-Layer Graphene by Shear Exfoliation in Liquids. *Nature Materials 2014 13:6* **2014**, *13* (6), 624−630.

(43) Yi, Z.; Su, F.; Cui, G.; Han, P.; Dong, N.; Chen, C. Computational Insights into the Interaction between Li2S/Li2S2 and Heteroatom-Doped Graphene Materials. *ChemistrySelect* **2019**, *4* (43), 12612−12621.

(44) Gong, Y.; Ma, W.; Xu, Z.; Wang, Y. Understanding the Interaction of N-Doped Graphene and Sulfur Compounds in a Lithium-Sulfur Battery: A Density Functional Theory Investigation. *New J. Chem.* **2022**, *46* (25), 12300−12310.

(45) Yin, L. C.; Liang, J.; Zhou, G. M.; Li, F.; Saito, R.; Cheng, H. M. Understanding the Interactions between Lithium Polysulfides and N-Doped Graphene Using Density Functional Theory Calculations. *Nano Energy* **2016**, *25*, 203−210.

(46) Mou, Z.; Chen, X.; Du, Y.; Wang, X.; Yang, P.; Wang, S. Forming Mechanism of Nitrogen Doped Graphene Prepared by Thermal Solid-State Reaction of Graphite Oxide and Urea. *Appl. Surf. Sci.* **2011**, *258* (5), 1704−1710.

(47) Hummers, W. S.; Offeman, R. E. Preparation of Graphitic Oxide. *J. Am. Chem. Soc.* **1958**, *80* (6), 1339.

(48) Li, F.; Jiang, X.; Zhao, J.; Zhang, S. Graphene Oxide: A Promising Nanomaterial for Energy and Environmental Applications. *Nano Energy* **2015**, *16*, 488−515.

(49) Huang, X.; Wang, Z.; Knibbe, R.; Luo, B.; Ahad, S. A.; Sun, D.; Wang, L. Cyclic Voltammetry in Lithium-Sulfur Batteries—Challenges and Opportunities. *Energy Technology* **2019**, *7* (8), 1801001.

(50) Zhao, M. Q.; Liu, X. F.; Zhang, Q.; Tian, G. L.; Huang, J. Q.; Zhu, W.; Wei, F. Graphene/Single-Walled Carbon Nanotube Hybrids: One-Step Catalytic Growth and Applications for High-Rate Li-S Batteries. *ACS Nano* **2012**, *6* (12), 10759−10769.

(51) Mačák, M.; Vyroubal, P.; Kazda, T.; Jaššo, K. Numerical Investigation of Lithium-Sulfur Batteries by Cyclic Voltammetry. *J. Energy Storage* **2020**, *27*, 101158.

(52) Narayanan, S. R.; Shen, D. H.; Surampudi, S.; Attia, A. I.; Halpert, G. Electrochemical Impedance Spectroscopy of Lithium-Titanium Disulfide Rechargeable Cells. *J. Electrochem. Soc.* **1993**, *140* (7), 1854−1861.

(53) Luo, Z.; Lim, S.; Tian, Z.; Shang, J.; Lai, L.; MacDonald, B.; Fu, C.; Shen, Z.; Yu, T.; Lin, J. Pyridinic N Doped Graphene: Synthesis, Electronic Structure, and Electrocatalytic Property. *J. Mater. Chem.* **2011**, *21* (22), 8038−8044.

(54) Kong, X. K.; Chen, Q. W. Improved Performance of Graphene Doped with Pyridinic N for Li-Ion Battery: A Density Functional Theory Model. *Phys. Chem. Chem. Phys.* **2013**, *15* (31), 12982−12987.

(55) Moy, D.; Manivannan, A.; Narayanan, S. R. Direct Measurement of Polysulfide Shuttle Current: A Window into Understanding the Performance of Lithium-Sulfur Cells. *J. Electrochem. Soc.* **2015**, *162* (1), A1−A7.

(56) Barchasz, C.; Molton, F.; Duboc, C.; Leprêtre, J. C.; Patoux, S.; Alloin, F. Lithium/Sulfur Cell Discharge Mechanism: An Original Approach for Intermediate Species Identification. *Anal. Chem.* **2012**, *84* (9), 3973−3980.

(57) Fan, F. Y.; Carter, W. C.; Chiang, Y. M. Mechanism and Kinetics of Li2S Precipitation in Lithium-Sulfur Batteries. *Adv. Mater.* **2015**, *27* (35), 5203−5209.

(58) Kim, J. M.; Engelhard, M. H.; Lu, B.; Xu, Y.; Tan, S.; Matthews, B. E.; Tripathi, S.; Cao, X.; Niu, C.; Hu, E.; Bak, S. M.; Wang, C.; Meng, Y. S.; Zhang, J. G.; Xu, W. High Current-Density-Charging Lithium Metal Batteries Enabled by Double-Layer Protected Lithium Metal Anode. *Adv. Funct. Mater.* **2022**, *32* (48), 2207172.

(59) Huang, Y.; Lin, L.; Zhang, C.; Liu, L.; Li, Y.; Qiao, Z.; Lin, J.; Wei, Q.; Wang, L.; Xie, Q.; Peng, D. L. Recent Advances and Strategies toward Polysulfides Shuttle Inhibition for High-Performance Li-S Batteries. *Advanced Science* **2022**, *9* (12), 2106004.

(60) Li, S.; Zhang, W.; Zheng, J.; Lv, M.; Song, H.; Du, L. Inhibition of Polysulfide Shuttles in Li-S Batteries: Modified Separators and Solid-State Electrolytes. *Adv. Energy Mater.* **2021**, *11* (2), 2000779.

(61) Gu, S.; Sun, C.; Xu, D.; Lu, Y.; Jin, J.; Wen, Z. Recent Progress in Liquid Electrolyte-Based Li-S Batteries: Shuttle Problem and Solutions. *Electrochemical Energy Reviews* **2018**, *1* (4), 599−624.

(62) Jeon, T.; Lee, Y. C.; Hwang, J. Y.; Choi, B. C.; Lee, S.; Jung, S. C. Strong Lithium-Polysulfide Anchoring Effect of Amorphous Carbon for Lithium-Sulfur Batteries. *Curr. Appl. Phys.* **2021**, *22*, 94−103.

(63) Fang, M.; Liu, X.; Ren, J. C.; Yang, S.; Su, G.; Fang, Q.; Lai, J.; Li, S.; Liu, W. Revisiting the Anchoring Behavior in Lithium-Sulfur Batteries: Many-Body Effect on the Suppression of Shuttle Effect. *npj Computational Materials* **2020**, *6* (1), 1−6.

(64) Zhang, L.; Liang, P.; Man, X.; Wang, D.; Huang, J.; Shu, H. bo; Liu, Z.; Wang, L. Fe, N Co-Doped Graphene as a Multi-Functional Anchor Material for Lithium-Sulfur Battery. *J. Phys. Chem. Solids* **2019**, *126*, 280−286.

(65) Perdew, J. P.; Burke, K.; Ernzerhof, M. Generalized Gradient Approximation Made Simple. *Phys. Rev. Lett.* **1996**, *77* (18), 3865.

(66) Vandevondele, J.; Krack, M.; Mohamed, F.; Parrinello, M.; Chassaing, T.; Hutter, J. Quickstep: Fast and Accurate Density Functional Calculations Using a Mixed Gaussian and Plane Waves Approach. *Comput. Phys. Commun.* **2005**, *167* (2), 103−128.

(67) Goedecker, S.; Teter, M.; Hutter, J. Separable Dual-Space Gaussian Pseudopotentials. *Phys. Rev. B* **1996**, *54* (3), 1703.

(68) VandeVondele, J.; Hutter, J. Gaussian Basis Sets for Accurate Calculations on Molecular Systems in Gas and Condensed Phases. *J. Chem. Phys.* **2007**, DOI: 10.1063/1.2770708.

(69) Grimme, S. Semiempirical GGA-Type Density Functional Constructed with a Long-Range Dispersion Correction. *J. Comput. Chem.* **2006**, *27* (15), 1787−1799.

(70) Sanville, E.; Kenny, S. D.; Smith, R.; Henkelman, G. Improved Grid-Based Algorithm for Bader Charge Allocation. *J. Comput. Chem.* **2007**, *28* (5), 899−908.